

Fast three-dimensional imaging of gold nanoparticles in living cells with photothermal optical lock-in Optical Coherence Microscopy

Christophe Pache,^{1*} Noelia L. Bocchio,¹ Arno Bouwens,¹ Martin Villiger,^{1,2} Corinne Berclaz,¹ Joan Goulley,³ Matthew I. Gibson,⁴ Christian Santschi,⁵ and Theo Lasser¹

¹ *Laboratoire d'Optique Biomédicale, Ecole Polytechnique Fédérale de Lausanne, Lausanne, Switzerland*

² *Current address: Wellman Center for Photomedicine, Massachusetts General Hospital, Boston, MA 02114 USA*

³ *ISREC, Ecole Polytechnique Fédérale de Lausanne, Lausanne, Switzerland*

⁴ *Department of Chemistry, University of Warwick, Coventry, CV4 7AL, UK*

⁵ *Nanophotonics and Metrology Laboratory, Ecole Polytechnique Fédérale de Lausanne, Lausanne, Switzerland*

*christophe.pache@epfl.ch

<http://lob.epfl.ch>

Abstract: We introduce photothermal optical lock-in Optical Coherence Microscopy (poli-OCM), a volumetric imaging technique, which combines the depth sectioning of OCM with the high sensitivity of photothermal microscopy while maintaining the fast acquisition speed inherent to OCM. We report on the detection of single 40 nm gold particles with a 0.5 μm lateral and 2 μm axial resolution over a 50 μm depth of field and the three-dimensional localization of gold colloids within living cells. In combination with intrinsic sample contrast measured with dark-field OCM, poli-OCM offers a versatile platform for functional cell imaging.

© 2012 Optical Society of America

OCIS codes: (110.3175, 110.6955) Imaging systems; (170.1530, 170.6900) Medical optics and biotechnology; (180.1655) Microscopy.

References and links

1. R. Weissleder and U. Mahmood, "Molecular imaging," *Radiology* **219**, 316–333 (2001).
2. J. Vogelsang, R. Kasper, C. Steinhauer, B. Person, M. Heilemann, M. Sauer, and P. Tinnefeld, "A reducing and oxidizing system minimizes photobleaching and blinking of fluorescent dyes," *Angew. Chem. Int. Ed.* **47**, 5465–5469 (2008).
3. C. J. Murphy, A. M. Gole, J. W. Stone, P. N. Sisco, A. M. Alkilany, E. C. Goldsmith, and S. C. Baxter, "Gold nanoparticles in biology: beyond toxicity to cellular imaging," *Accounts Chem. Res.* **41**, 1721–1730 (2008).
4. M. Celebrano, P. Kukura, A. Renn, and V. Sandoghdar, "Single-molecule imaging by optical absorption," *Nat. Photonics* **5**, 95–98 (2011).
5. U. Resch-Genger, M. Grabolle, S. Cavaliere-Jaricot, R. Nitschke, and T. Nann, "Quantum dots versus organic dyes as fluorescent labels," *Nat. Methods* **5**, 763–775 (2008).
6. D. Boyer, P. Tamarat, A. Maali, B. Lounis, and M. Orrit, "Photothermal imaging of nanometer-sized metal particles among scatterers," *Science* **297**, 1160–1163 (2002).
7. S. Berciaud, L. Cognet, G. Blab, and B. Lounis, "Photothermal heterodyne imaging of individual nonfluorescent nanoclusters and nanocrystals," *Phys. Rev. Lett.* **93**, 257402 (2004).

8. L. Novotny and B. Hecht, *Principles of Nano-Optics* (Cambridge University Press, 2012).
9. J. Kim, J. Oh, H. W. Kang, M. D. Feldman, and T. E. Milner, "Photothermal response of superparamagnetic iron oxide nanoparticles," *Laser Surg. Med.* **40**, 415–421 (2008).
10. D. Lasne, G. A. Blab, F. De Giorgi, F. Ichas, B. Lounis, and L. Cognet, "Label-free optical imaging of mitochondria in live cells," *Opt. Express* **15**, 14184–14193 (2007).
11. S. Lu, W. Min, S. Chong, G. R. Holtom, and X. S. Xie, "Label-free imaging of heme proteins with two-photon excited photothermal lens microscopy," *Appl. Phys. Lett.* **96**, 113701 (2010).
12. A. Gaiduk, P. V. Ruijgrok, M. Yorulmaz, and M. Orrit, "Detection limits in photothermal microscopy," *Chem. Sci.* **1**, 343–350 (2010).
13. A. Fercher, W. Drexler, C. Hitzenberger, and T. Lasser, "Optical coherence tomography - principles and applications," *Rep. Prog. Phys.* **66**, 239–303 (2003).
14. J. Izatt, M. Hee, G. Owen, E. Swanson, and J. Fujimoto, "Optical coherence microscopy in scattering media," *Opt. Lett.* **19**, 590–592 (1994).
15. A. K. Ellerbee, T. L. Creazzo, and J. A. Izatt, "Investigating nanoscale cellular dynamics with cross-sectional spectral domain phase microscopy," *Opt. Express* **15**, 8115–8124 (2007).
16. C. Joo, C. L. Evans, T. Stepinac, T. Hasan, and J. F. de Boer, "Diffusive and directional intracellular dynamics measured by field-based dynamic light scattering," *Opt. Express* **18**, 2858–2871 (2010).
17. M. Villiger, C. Pache, and T. Lasser, "Dark-field optical coherence microscopy," *Opt. Lett.* **35**, 3489–3491 (2010).
18. J.-A. Conchello and J. W. Lichtman, "Optical sectioning microscopy," *Nat. Meth.* **2**, 920–931 (2005).
19. A. S. Paranjape, R. Kuranov, S. Baranov, L. L. Ma, J. W. Villard, T. Wang, K. V. Sokolov, M. D. Feldman, K. P. Johnston, and T. E. Milner, "Depth resolved photothermal OCT detection of macrophages in tissue using nanorose," *Biomed. Opt. Express* **1**, 2–16 (2010).
20. M. C. Skala, M. J. Crow, A. Wax, and J. A. Izatt, "Photothermal Optical coherence tomography of epidermal growth factor receptor in live cells using immunotargeted gold nanospheres," *Nano Lett.* **8**, 3461–3467 (2008).
21. C. Zhou, T.-H. Tsai, D. C. Adler, H.-C. Lee, D. W. Cohen, A. Mondelblatt, Y. Wang, J. L. Connolly, and J. G. Fujimoto, "Photothermal optical coherence tomography in ex vivo human breast tissues using gold nanoshells," *Opt. Lett.* **35**, 700–702 (2010).
22. Y. Jung, R. Reif, Y. Zeng, and R. K. Wang, "Three-dimensional high-resolution imaging of gold nanorods uptake in sentinel lymph nodes," *Nano Lett.* **11**, 2938–2943 (2011).
23. E. Absil, G. Tessier, M. Gross, M. Atlan, N. Wanasooriya, S. Suck, M. Coppey-Moisand, and D. Fournier, "Photothermal heterodyne holography of gold nanoparticles," *Opt. Express* **18**, 780–786 (2010).
24. D. C. Adler, S.-W. Huang, R. Huber, and J. G. Fujimoto, "Photothermal detection of gold nanoparticles using phase-sensitive optical coherence tomography," *Opt. Express* **16**, 4376–4393 (2008).
25. J. Izatt and M. Choma, "Theory of optical coherence tomography," in *Optical coherence tomography*, W. Drexler, ed. (Springer Verlag, 2008), pp. 47–72.
26. R. Leitgeb, C. Hitzenberger, and A. Fercher, "Performance of Fourier domain vs. time domain optical coherence tomography," *Opt. Express* **11**, 889–894 (2003).
27. R. A. Leitgeb, M. Villiger, A. H. Bachmann, L. Steinmann, and T. Lasser, "Extended focus depth for Fourier domain optical coherence microscopy," *Opt. Lett.* **31**, 2450–2452 (2006).
28. M. Villiger and T. Lasser, "Image formation and tomogram reconstruction in optical coherence microscopy," *J. Opt. Soc. Am. A* **27**, 2216–2228 (2010).
29. V. Kodach, N. Bosschaart, and J. Kalkman, "Concentration dependent scattering coefficients of intralipid measured with OCT," in "Biomedical Optics," OSA Technical Digest (CD) (Optical Society of America, 2010), paper B5uD11.
30. M. Leutenegger, R. Rao, R. A. Leitgeb, and T. Lasser, "Fast focus field calculations," *Opt. Express* **14**, 11277–11291 (2006).
31. R. Herman and T. Wiggins, "Production and uses of diffractionless beams," *J. Opt. Soc. Am. A* **8**, 932–942 (1991).
32. D. McGloin and K. Dholakia, "Bessel beams: diffraction in a new light," *Contemp. Phys.* **46**, 15–28 (2005).
33. S. Boppart, A. Oldenburg, C. Xu, and D. Marks, "Optical probes and techniques for molecular contrast enhancement in coherence imaging," *J. Biomed. Opt.* **10**, 041208 (2005).
34. A. Oldenburg, F. Touban, K. Suslick, A. Wei, and S. Boppart, "Magnetomotive contrast for in vivo optical coherence tomography," *Opt. Express* **13**, 6597–6614 (2005).
35. V. Crecea, A. L. Oldenburg, X. Liang, T. S. Ralston, and S. A. Boppart, "Magnetomotive nanoparticle transducers for optical rheology of viscoelastic materials," *Opt. Express* **17**, 23114–23122 (2009).
36. M. Wagner, P. Weber, T. Bruns, W. S. L. Strauss, R. Wittig, and H. Schneckenburger, "Light dose is a limiting factor to maintain cell viability in fluorescence microscopy and single molecule detection," *Int. J. Mol. Sci.* **11**, 956–966 (2010).

1. Introduction

Molecular imaging plays a fundamental role in today's research in biology and medicine [1]. It relies on compounds (antibodies, peptides, etc.) that specifically target a molecule of interest in an organism and use a reporting mechanism to generate a detectable signal. In the field of optical imaging and microscopy, fluorescent dyes are the most common exogenous labels. They can be linked to the molecules of interest, or - as in the case of fluorescent proteins - they can be endogenously expressed. Fluorescence microscopy is a mature technique that has revolutionized the understanding of biological processes and structures at the microscopic level. However, fluorescent markers suffer, despite all efforts to increase their stability [2], from inherent photobleaching which hinders long-term studies. Many alternative approaches, relying on other optical properties such as scattering [3] or absorption [4], have been proposed to solve this issue [5]. Among these, photothermal microscopy stands out as a very promising alternative [6,7]. Instead of relying on the re-emission of a Stokes-shifted fluorescence signal, this technique exploits the local heating induced in the sample by the primary absorption of an extrinsic label. Illuminated by a time-modulated heating or pump beam, a small nano-sized absorber induces a variation of temperature in its proximity and, in turn, a variation of the refractive index. A probe beam of a different wavelength generates a scattering signal that is modulated by the photothermal effect and is detected and demodulated with a lock-in amplifier, conferring an excellent sensitivity to the method. The probe and heating beams are superposed and raster scanned over the object in a confocal approach. Prominent absorbers that meet the requirements for optical labelling are, e.g. gold nanoparticles (AuNPs), particularly when close to their plasmon resonance [8], and iron oxide nanoparticles - an FDA approved nanomaterial [9] - among others. What is more, intrinsic contrast from absorbing molecules such as hemoglobin or proteins contained in mitochondria has also been examined in living biological samples [10, 11]. The sensitivity of this method is such that even the detection of single molecules has been reported [12].

Optical Coherence Microscopy (OCM), the microscopic counterpart of Optical Coherence Tomography (OCT) [13], measures backscattered light with very high sensitivity and provides cross-sectional views of the subsurface microstructure of biological tissue, with a high axial and lateral resolution of 2-3 μm [14]. Furthermore, it gives access to both amplitude and phase of the scattered light and has been successfully applied to functional cell imaging [15, 16]. Recently, we reported on a dark-field configuration for OCM (dfOCM) that offers enhanced sensitivity to very weak scattering signals and enables transparent cell samples to be imaged with high contrast [17].

Variations of the refractive index are the intrinsic source of contrast for OCM and hence, OCM appears to be particularly well suited for photothermal imaging. Moreover, OCM allows high acquisition rate that can provide 3D images of a scanned area within seconds, in contrast to e.g. confocal microscopy, which can take several minutes under comparable conditions [18]. The fast volumetric imaging of OCM and the high sensitivity to extrinsic labels of photothermal imaging call for a combination of these two approaches to complement the intrinsic contrast measured by OCM with a specific signal of the photothermal label. Several groups have already explored photothermal signals using OCT [19–22]. However, in order to obtain an exploitable contrast from AuNPs, all the proposed solutions compromised the speed advantage of OCT: the photothermal signal was extracted from the Fourier transform of the phase signal recorded over time, which required the acquisition of multiple axial profiles at the same lateral position. In addition, only highly concentrated solutions of relatively large nanoparticles (30 to 120 nm) provided detectable signals. Another interesting approach based on digital holography reported on the heterodyne detection of single gold particles down to a diameter of 10 nm [23]. However, the photothermal signal arose only in a small sub-area of the available field of view (FOV) and although depth sectioning was demonstrated, no three-dimensional localization of AuNPs was

shown.

Here, we propose photothermal optical lock-in OCM (poli-OCM), an approach that combines the depth sectioning of OCM with the high sensitivity of the lock-in detection of photothermal microscopy without compromising the acquisition speed inherent to OCM. The principle idea is to modulate the phase of the reference signal in order to capture exclusively the signal variation induced by the photothermal effect. The integration time of the spectrometer's CCD camera acts as a low-pass filter and isolates the demodulated signal from the high frequency background signal. Our dfOCM setup was equipped with a photothermal excitation path, along with its dedicated lock-in detection. The setup can switch from a dfOCM mode to poli-OCM on demand.

2. Theory

As derived by Berciaud et al. [7], the refractive index variation of a medium surrounding a point-shaped absorber, heated with a sinusoidal modulation at the angular frequency Ω can be described as

$$\Delta n(r, t) = \frac{\partial n}{\partial T} \frac{P_{abs}}{4\pi\kappa r} \left[1 + \cos(\Omega t - \frac{r}{r_{th}}) e^{-r/r_{th}} \right] \quad (1)$$

where P_{abs} is the power absorbed by the particle, r the distance from the particle, n the index of refraction of the medium, $\partial n/\partial T$ its variation with temperature and $r_{th} = [2\kappa/(\Omega C_p)]^{1/2}$ the characteristic length for heat diffusion, with κ representing the thermal conductivity of the medium and C_p its heat capacity per unit volume. In combination with the thermal expansion of the medium, this change of refractive index produces both a static and a dynamic change of the optical path length [24]. The dynamic term is the one of interest here, as its frequency signature enables an efficient lock-in detection. To simplify, we assume that the light backscattered by a region surrounding a heated nanoparticle experiences a phase modulation at the excitation frequency. In the framework of a classical OCT model [25], the scattered field by a sample consisting of N backscattering layers and a single AuNP can be written as

$$E_s(k, t) = E_i \sum_{n=1}^N r_n e^{i2kz_n} + E_i r_{np} e^{ik[2z_{np} + \alpha \cos(\Omega t)]} = E_{df} + E_{poli} \quad (2)$$

where r_n and z_n stand for the electric field reflectivity and position of each layer n . The AuNP reflectivity and position are represented by r_{np} and z_{np} . We separated the sample field E_s in a non-absorbing field contribution E_{df} (sum term) and an absorbing field contribution E_{poli} caused by the single nanoparticle absorption (this restriction to a single AuNP is only done for the sake of clarity and implies no limitation to the model). E_{df} and E_{poli} correspond to the scattered fields detected in the dfOCM and poli-OCM modes respectively. E_i represents the field amplitude of the incident light on the sample. The angular modulation frequency of the heating beam is Ω and α stands for the induced path length modulation.

The scattered field E_s will then interfere with the reference field E_r . By placing two acousto-optic modulators in the reference arm, this field can be temporally modulated in phase and corresponds to

$$E_r(k, t) = E_i r_r e^{i2kz_r} e^{-i(\Omega t + \varphi)} \quad (3)$$

where φ represents a fixed phase delay between the modulation of the heating beam intensity and the reference phase, r_r the reference arm reflectivity and z_r the optical path length of the reference arm. The interfering intensity per k-channel at the exit of the interferometer is then given as

$$I_{det}(k, t) = (E_r + E_{df} + E_{poli})(E_r + E_{df} + E_{poli})^*. \quad (4)$$

A straightforward multiplication leads to 9 terms which can be further combined into a constant DC contribution, a negligible autocorrelation contribution and the terms of interest i.e. the cross-correlation between the modulated reference field and the sample field. This last contribution can be split into two terms: a poli-OCM signal I_{poli} (interference between E_r and E_{poli}) and a dfOCM signal I_{df} (interference between E_r and E_{df})

$$I_{poli}(k, t) = E_r E_{poli}^* + E_r^* E_{poli} = E_i^2 r_r r_{np} e^{i2k(z_r - z_{np})} e^{-i[\Omega t + \varphi + \alpha k \cos(\Omega t)]} + c.c. \quad (5)$$

$$I_{df}(k, t) = E_r E_{df}^* + E_r^* E_{df} = E_i^2 \Phi_{df}(k) e^{-i(\Omega t + \varphi)} + c.c. \quad (6)$$

where $\Phi_{df}(k) = \Phi_{df}(k; z_r, z_n, r_r, r_n)$ contains all the non-time dependent contributions. The interference signal $I_{df}(k, t)$ from a non heated region within the sample acts as background for the poli-OCM mode. Setting the integration time of the line camera to an integer multiple m of periods of the modulation frequency, the integrated background will no longer contribute to the final signal. For an integration time $\tau = m\Delta t$ where m is an integer and $\Delta t = 2\pi/\Omega$ represents one modulation period, we can write

$$\langle I_{df}(k, t) \rangle = e^{-i\varphi} E_i^2 \Phi_{df}(k) \int_0^\tau e^{-i\Omega t} dt + c.c. = 0. \quad (7)$$

On the other hand, part of a scattering term modulated by the photothermal effect will be demodulated by the reference beam and result in net signal

$$\langle I_{poli}(k, t) \rangle = e^{-i\varphi} E_i^2 r_r r_{np} e^{i2k(z_r - z_{np})} \int_0^\tau e^{-i[\alpha k \cos(\Omega t) + \Omega t]} dt + c.c. \quad (8)$$

This integral can be further simplified with the Jacobi-Anger expansion:

$$e^{i\beta \cos \Theta} = \sum_{n=-\infty}^{\infty} i^n J_n(\beta) e^{in\Theta}. \quad (9)$$

By identifying the coefficient $\beta = -\alpha k$, the integral can be rewritten as

$$\int_0^\tau e^{-i[\alpha k \cos(\Omega t) + \Omega t]} dt = \sum_{n=-\infty}^{\infty} i^n J_n(-\alpha k) \int_0^\tau e^{i[n\Omega t - \Omega t]} dt \quad (10)$$

where the integral term can be split into two cases

$$\int_0^\tau e^{i[n\Omega t - \Omega t]} dt = \begin{cases} \tau, & n = 1 \\ 0, & n \neq 1 \end{cases} \quad (11)$$

This finally leads to

$$\langle I_{poli}(k, t) \rangle = i e^{-i\varphi} E_i^2 r_r r_{np} \tau e^{i2k(z_r - z_{np})} J_1(-\alpha k) + c.c. \quad (12)$$

$$= E_i^2 r_r r_{np} \tau \cdot 2J_1(\alpha k) \sin[2k(z_r - z_{np}) - \varphi] \quad (13)$$

$$\approx E_i^2 r_r r_{np} \tau \cdot \alpha k \sin[2k(z_r - z_{np}) - \varphi], \quad \text{if } \alpha k \ll 1. \quad (14)$$

Under typical experimental conditions, we estimate αk to be on the order of 10^{-3} . The tomogram $S(z)$ is derived in a standard manner [25, 26] from the Fourier transform of $\langle I_{poli}(k, t) \rangle$. The constant phase shift φ does not have any effect on the tomogram amplitude. At the given depth $z = z_{np}$, the amplitude of the signal can then be written as

$$|S(z_{np})| \propto \alpha \tau r_{np} r_r \sqrt{P_s P_r} \quad (15)$$

where P_s and P_r indicate respectively the power incident onto the sample and the power at the input of the reference arm.

Following Gaiduk et al. [12], we assume the photothermal effect (identified here by α) to be proportional to the volume integral of the refractive index variation surrounding the nanoparticle. They showed that the volume integral of the time varying part of this equation is proportional to $\partial n / \partial T \cdot [P_{abs} / (\Omega C_p)]$. In order to optimize the detection of the photothermal signal, the thermal radius r_{th} is matched with the waist of the probe beam, by optimizing the modulation frequency. In a given cell sample, the only tunable parameter remaining is the heating power P_{heat} in the object plane, hence $\alpha \propto P_{heat}$ and the absorption cross-section of the AuNP relates P_{abs} to P_{heat} .

Assuming a shot-noise limited performance, the noise variance is described as

$$\sigma_N^2 \propto \tau(r_{np}^2 P_s + r_r^2 P_r) \approx \tau r_r^2 P_r, \quad \text{as } r_{np}^2 P_s < r_r^2 P_r. \quad (16)$$

Following the seminal work of Leitgeb et al. [26], we obtain for the SNR in OCM:

$$SNR = \frac{|S(z_{np})|^2}{\sigma_N^2} \propto \frac{(P_{heat} \tau r_{np} r_r \sqrt{P_s P_r})^2}{\tau r_r^2 P_r} = \tau r_{np}^2 P_s P_{heat}^2. \quad (17)$$

For a shot-noise limited performance, the SNR of poli-OCM is proportional to the integration time τ , the probe power incident onto the sample P_s and the squared power of the heating beam P_{heat} .

3. Experimental

Figure 1(a) depicts the schematic of the poli-OCM setup. Based on a Mach-Zehnder interferometer, it corresponds to a modified FDOCM concept with decoupled illumination and detection apertures [27].

At the output of the illumination fiber (mode field diameter of 4.2 μm , single mode polarization maintaining fiber, Fibercore Ltd., England), light from a broadband source (Ti-Sa laser, Femtolasers Inc., Austria) with a central wavelength at 800 nm and full-width at half maximum bandwidth of 135 nm (providing a 2 μm axial resolution in aqueous medium) is first collimated and split into the reference and illumination arms. Two tellurium dioxide crystals placed in the collimated illumination beam compensate for the dispersion of the two acousto-optic modulators in the reference arm, whereas glass (BK7) prisms located in the reference path compensate for all other optical components (objective, tube lens and scanning lens) of the illumination/detection paths. An axicon (176° apex angle, Del Mar Photonics Inc., USA) produces a radial zero-order Bessel beam, which is then imaged in the object focal plane by three consecutive 4-f systems. To optimize the dark-field effect, an illumination mask F_{ill} , placed in the first telescope, blocks the parasitic light, mainly generated by the axicon tip. The inverted microscope consists of a 164 mm tube lens (Carl Zeiss, Germany) and a Zeiss plan apochromat immersion objective (25x, NA 0.8). The overall interferometer corresponds to a so-called Bessel-Gauss configuration [28], i.e. the backscattered light (signal) is superimposed with the reference light and focused into a single mode fiber (mode field diameter of 4.6 μm , Corning Inc., USA). This fiber redirects the collected signal to the spectrometer. A circular aperture F_{det} in the collimated part of the detection path reduces the detection NA such that specular reflection of the illumination field on planar interfaces within the object space is largely suppressed. This represents the essence of the dark-field mode in OCM.

The illumination field follows a radial zero-order Bessel distribution in the focal plane with the first minimum located at 0.41 μm , whereas the detection mode is Gaussian with a reduced numerical aperture (NA) of about 0.18. A dichroic mirror placed in front of the scanning system in the illumination path redirects the heating beam (effective NA of 0.19) onto the sample,

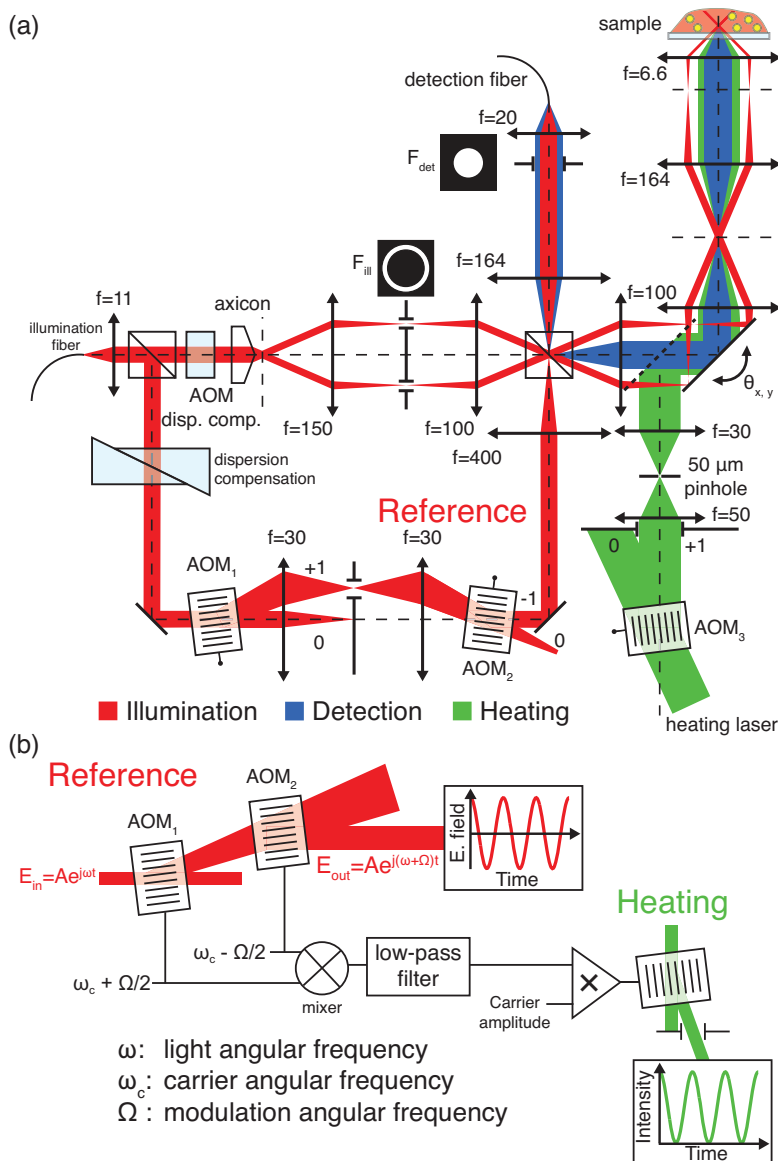


Fig. 1. (a) Schematic of the poli-OCM setup. The intensity modulation of the heating beam and the phase modulation of the reference beam are performed by acousto-optic modulators (AOM). The interferometer is in a Bessel-Gauss configuration: the Bessel illumination is created by the use of an axicon, whereas the detection remains a Gaussian mode, producing a dark-field effect. (b) Diagram of the electronic synchronization of the reference phase and heating intensity modulations.

collinear with the illumination mode. Before entering the system, an acousto-optic modulator AOM_3 (MT110-A1.5-VIS, AA Inc., France) imprints a sinusoidal intensity modulation at the angular frequency Ω onto the heating beam (532 nm, diode pumped solid state laser, Roithner Lasertechnik Inc., Austria). The beam is filtered by a 50 μm pinhole placed inside a Kepler telescope. The two collinear beams are raster scanned across the object. The two AOMs (MT110-B50AI-IR, AA Inc., France) in the reference arm are driven at a common carrier angular frequency but with a small upward shift of $+\Omega/2$ on AOM_1 and downward shift of $-\Omega/2$ on AOM_2 , producing a phase modulation of the reference field at the beating angular frequency Ω . A telescope placed in-between AOM_1 and AOM_2 compensates for chromatic dispersion.

In order to ensure the lock-in detection, the heating intensity modulation is synchronized with this beating frequency (see Fig. 1(b)). First, an electronic mixer combines the two AOM driving signals. A low-pass filter extracts the beating angular frequency Ω out of the composite signal, which drives the amplitude of the carrier signal of AOM_3 .

Light backscattered by the sample is recombined with the reference field by a single mode detection fiber and the resulting interference pattern is recorded by a spectrometer (transmission grating 1200 lines/mm, $f=135$ mm, Atmel Aviva M2 line detector). The sample axial structure is extracted by computing the fast Fourier transform (FFT) of the measured spectrum, after interpolating in k-space and subtracting the average background.

For the evaluation of the SNR, the noise variance σ_N^2 is measured at the same depth position as the signal but in a tomogram where only the reference arm was recorded over time (by blocking the sample arm). This manner of measuring the noise offers the advantage of taking into account the sensitivity roll-off of the spectrometer. The tomograms are displayed on a logarithmic scale (dB), corresponding to $10 \cdot \log_{10}$ of the squared amplitude of the FFT.

In the present study, the typical integration time was set to 250 μs with a line rate of 3.9 kHz and the optimized modulation frequency was fixed to 152 kHz. The imaging mode could be switched on demand from poli-OCM to dfOCM by setting Ω to zero, which blocks the heating beam. The sample was illuminated with 5 mW for the probe beam (P_s) and depending on the experiment, the heating beam power P_{heat} was varied between 10 and 65 mW, corresponding to an intensity of 230 to 1500 kW/cm².

4. Results

The selective contrast of poli-OCM was first evaluated on 40 nm AuNPs embedded in a highly scattering medium. Next the three-dimensional imaging capability of poli-OCM was assessed. The dependency of the SNR on the integration time and heating intensity was also measured according to our theoretical analysis (see Eq. 17). Finally, we applied this overall concept to in vitro cell imaging of HeLa cells loaded with AuNPs (6 nm diameter).

4.1. Photothermal contrast

The photothermal contrast of poli-OCM was first verified by discriminating AuNPs from highly concentrated scatterers. Gold nanodiscs of 40 nm in diameter and height were fabricated by e-beam lithography combined with a subsequent lift-off process on a microscope coverslide and immersed in a drop of intravenous perfusion fluid (Lipovenös 20%, Fresenius Kabi Inc., Switzerland). The scattering coefficient μ_s of this intralipid [29] was estimated to be 18 mm⁻¹. The discs were produced in a square array with a disc-to-disc separation of 10 μm to ensure a single particle detection.

Figure 2(a) and 2(b) correspond to the en-face views at the axial position of the particles in both dfOCM and poli-OCM respectively. Figure 2(d) and 2(e) show the cross-section (B-scan) along the line indicated in Fig. 2(a) and 2(b). The tomogram recorded with dfOCM features speckle due to the scattering within the intralipid solution; no signal from the gold nanoparticles

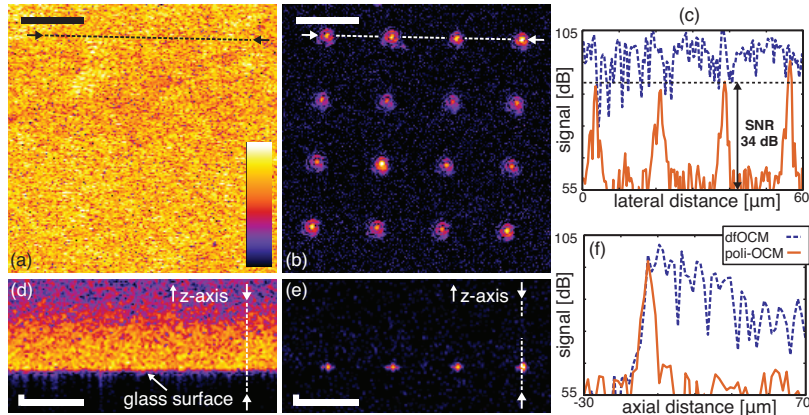


Fig. 2. Demonstration of the contrast selective to gold nanoparticles offered by poli-OCM, as compared to dfOCM. A square lattice of isolated 40 nm gold particles on a glass surface immersed in intravenous perfusion fluid, imaged with dfOCM (a), and poli-OCM (b). (d) and (e) correspond to cross-sections along the lines indicated in (a) and (b); Graph (c) depicts the signal along the lines in (a) and (b), while (f) corresponds to the axial signal along the line highlighted in (d) and (e). Scale bars: 10 μm .

can be identified in this measurement. The selective contrast of poli-OCM is clearly evidenced in Fig. 2(b), where the background signal is completely suppressed and the gold nanoparticles are visible. The dfOCM tomogram in Fig. 2(a) and 2(d) is displayed within a range of 45 dB, whereas the poli-OCM tomogram in Fig. 2(b) and 2(e) was scaled to 35 dB. Figure 2(c) plots the signals along the lines indicated in Fig. 2(a) and 2(b). The mean SNR of a 40 nm gold particle in poli-OCM is about 34 dB, while the scattering signal of the same particle is entirely buried in the signal generated by intralipid in the dfOCM mode. Note that the signal from these non-absorbing scatterers, considered as background in the photothermal image, is completely suppressed by the modulation of the reference signal and the integration over a finite number of modulation periods. The axial profiles (A-scans, Fig. 2(f)) corresponding to the lines in between the arrows in Fig. 2(d) and 2(e), reveal the optical sectioning of poli-OCM as well as the strong attenuation of all background contributions. For these experiments, the intensity of the heating beam was set to 1500 kW/cm^2 .

4.2. Point spread function and depth of field

The characterization of the point spread function (PSF) and the depth of field (DOF) of both dfOCM and poli-OCM is paramount for assessing the three-dimensional imaging performance of these novel methods. In parallel to the measurements, we calculated the PSFs by the use of a fast focal field computation algorithm developed by Leutenegger et al. [30]. The algorithm computes the focal field based on the field distribution in the back aperture of the objective. This input field was computed taking into account the propagation across all optical components in the beam paths. As OCM is an interferometric imaging modality, it measures the field amplitude and not the intensity. Thus, the normalized field amplitudes, $E_{\text{ill}}(r, z)$ and $E_{\text{det}}(r, z)$, of the illumination and the detection were used to compute the PSF of dfOCM. On top of that, poli-OCM is sensitive to absorption by nanoparticles of the normalized heating beam intensity $I_{\text{heat}}(r, z)$. The Airy profile of the heating intensity was approximated by a Gaussian mode and

the following relations were used to compute the PSFs of both systems, where

$$PSF_{dfOCM} = E_{ill}(r, z) \cdot E_{det}(r, z) \quad (18)$$

$$PSF_{poli-OCM} = E_{ill}(r, z) \cdot E_{det}(r, z) \cdot I_{heat}(r, z). \quad (19)$$

The PSFs were again measured with the e-beam fabricated 40 nm particles and the same heating beam intensity but with the particles immersed in water instead of intralipid. The results are presented in Fig. 3, along with normalized theoretical values. Figure 3(a) and 3(c) reveal the

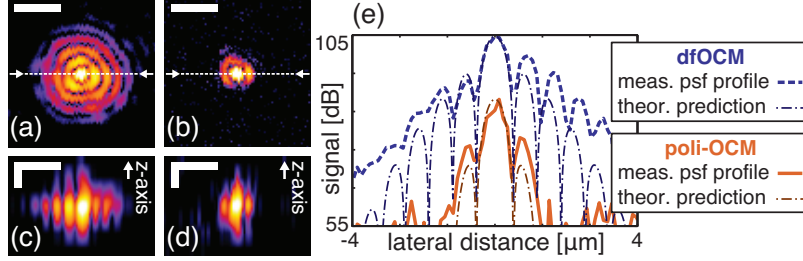


Fig. 3. In-focus point spread functions of poli-OCM and dfOCM. (a) in-focus en-face view of a single 40 nm gold nanoparticle with dfOCM; (b) poli-OCM, (c, d) B-scans along the line indicated in (a) and (b) and (e) lateral profiles along the same line in comparison with theoretical predictions. Scale bars: 3 μm.

dfOCM 3D field distribution (30 dB range) in an en-face view along with its cross-section. With poli-OCM, the same nanoparticle gives rise to the signal shown in Fig. 3(b) and 3(d) with 25 dB range. Figure 3(e) compares theoretical calculations to experimental results and shows good agreement. poli-OCM provides an additional resolution enhancement due to the interplay between the heating beam and the illumination/detection profiles of dfOCM.

The DOF was evaluated on tomograms of 6 nm gold particles dispersed in a polydimethylsiloxane (PDMS) matrix, with a heating intensity of 230 kW/cm² on the sample, corresponding to 10 mW. Figure 4(a) and 4(c) display maximum projections of the depth color-coded dfOCM

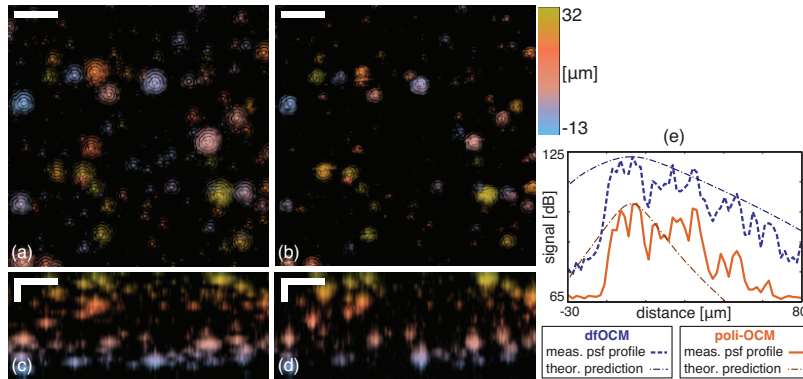


Fig. 4. Depth of field characterization of poli-OCM and dfOCM, with 6 nm gold particles dispersed in a polymer matrix. (a, c) display maximum amplitude projections of the depth color-coded dfOCM tomogram volume in xy (en-face) and yz (cross-section) planes, (b, d) poli-OCM, (e) presents the maximum signal in each xy section as a function of the depth, to estimate the DOF in dfOCM and poli-OCM. Scale bars: 10 μm.

tomogram volume (25 dB range), respectively in xy (en-face) and yz (cross-section) planes.

Figure 4(b) and 4(d) recorded with poli-OCM (30 dB range) indicate a good correlation with dfOCM, as well as a comparable DOF. The higher number of scatterers observed in the dfOCM images can be attributed to residual air bubbles or impurities trapped inside the PDMS. These structures cannot be seen in poli-OCM images as they are non-absorbing and thus, disappear. In order to quantify the DOF, the maximum signal level within the xy plane was extracted at each depth. The resulting curves are plotted in Fig. 4(e) and show that the poli-OCM provides a slightly larger DOF than expected from theoretical calculations. The measured DOF of dfOCM and poli-OCM is about 50 μm at full-width at half maximum. The lateral PSFs of both methods are nearly preserved over the full DOF, due to the extended focus known from Bessel beam propagation [31, 32]. Nevertheless, the enlargement of the Gaussian detection waist in out of focus positions contributes to the collection of higher side lobes. This results in a widening of the lateral PSFs along the axial distance, as observable in Fig. 4(c) and 4(d).

4.3. Signal-to-noise ratio

In order to confirm the theoretical analysis and determine the detection limits of poli-OCM, we measured the SNR in dependency of different parameters on 50 nm AuNPs dispersed in a polydimethylsiloxane (PDMS) matrix. For each integration time τ , the reference arm intensity was readjusted (by reducing the amount of collected light with a diaphragm) to about 70% of the available dynamic range of the linescan camera. These measurements are presented in Fig. 5. The linear increase of the SNR in function of the integration time (Fig. 5(a)), as well as with the probe power (Fig. 5(b)), attest of the shot-noise limited performance of poli-OCM. For other noise contributions (excess or receiver), these relations are not linear, as explained in the detailed analysis of Leitgeb et al. [26]. Finally, a good correspondence between the theory and the experiment is also observed for variations of the heating power (Fig. 5(c)).

4.4. Live cell imaging

In a last step, we applied poli-OCM in combination with dfOCM to three-dimensional imaging of living cells loaded with nanoparticles. HeLa cells were cultured in petri dishes and incubated overnight with a suspension of 6 nm AuNPs coated with a polyethylenglycol-based polymer in Dulbecco's modified Eagles's medium (DMEM) containing 450 mg/dl glucose, 10% fetal calf serum, penicillin and streptomycin antibiotics 1%. Cells were incubated at 37°C and 5% CO₂ to a confluence of approximately 40%. After incubation, the suspension was removed, the sample rinsed with phosphate buffered saline, and the dishes filled with fresh cell culture medium. Cells were imaged using dfOCM and poli-OCM with a heating power of 12 mW, resulting in an energy density of 57.5 J/cm² ($\tau=250$ μs). The results are summarized in Fig. 6. HeLa cells give rise to a strong signal in the dfOCM image (Fig. 6(a), 6(c) and 6(e); 30 dB range); as a result, gold nanoparticles cannot be differentiated from highly scattering components within the cells. In contrast, poli-OCM (Fig. 6(b), 6(d) and 6(f); 25 dB range) selectively images the AuNPs and reveals clearly their presence inside the cells. The maximum thickness of the cell in Fig. 6(e) is about 20 μm and nanoparticles can be detected over the whole axial extent by poli-OCM, as shown in Fig. 6(f). A 3D rendering of the same information is contained in the Fig. 6(g), where the blue semi-transparent surface represents the cells volume and the yellow content the AuNPs. A control experiment on living HeLa cells without nanoparticles proved that with the same imaging conditions (integration time, heating power, etc.), no intrinsic photothermal signal could be detected. After internalization, AuNPs seem to aggregate near the nucleus, as indicated in Fig. 6(d) and 6(f).

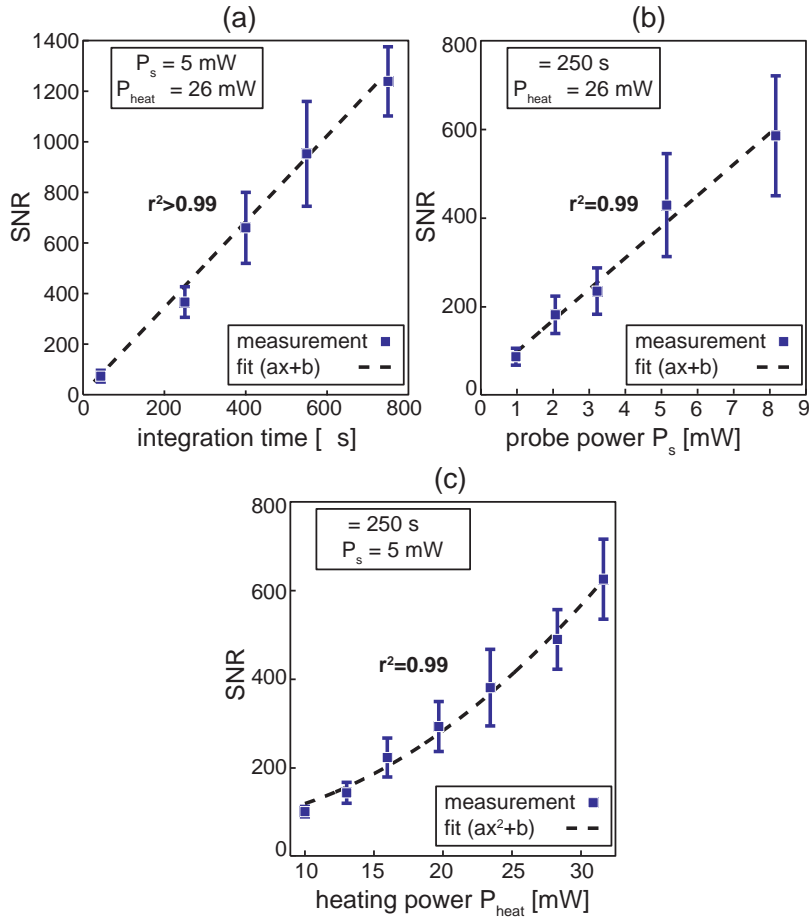


Fig. 5. (a) Mean SNR of one 50 nm gold particle in PDMS in function of the integration time τ , (b) the probe power P_s and (c), the heating power P_{heat} . Error bars show the standard deviation over 10 measurements.

5. Discussion

This work demonstrates that photothermal contrast can be efficiently applied to OCM with a lock-in detection scheme and thus, enables the three-dimensional imaging of probes with a high contrast and without affecting the fast acquisition speed inherent to OCT/OCM. Moreover, poli-OCM offers background free localization of AuNPs even in the presence of highly scattering media. The imaging mode can be switched from dfOCM to poli-OCM on demand, allowing the localization of absorbing objects within scattering structures detected with dfOCM. The characterization of the point spread functions of both methods revealed a resolution increase due to the photothermal contrast conferred by the apodization of the dfOCM PSF by the heating beam intensity, while the depth of field is almost preserved.

The linear increase of the SNR with the integration time, the probe power and with the square of the heating power was confirmed experimentally. This is consistent with previous studies [7, 12, 20, 23].

The heating intensities used in this study remain in the same order of magnitude as those employed by previous studies [7, 12], in contrast to photothermal OCT-based techniques that

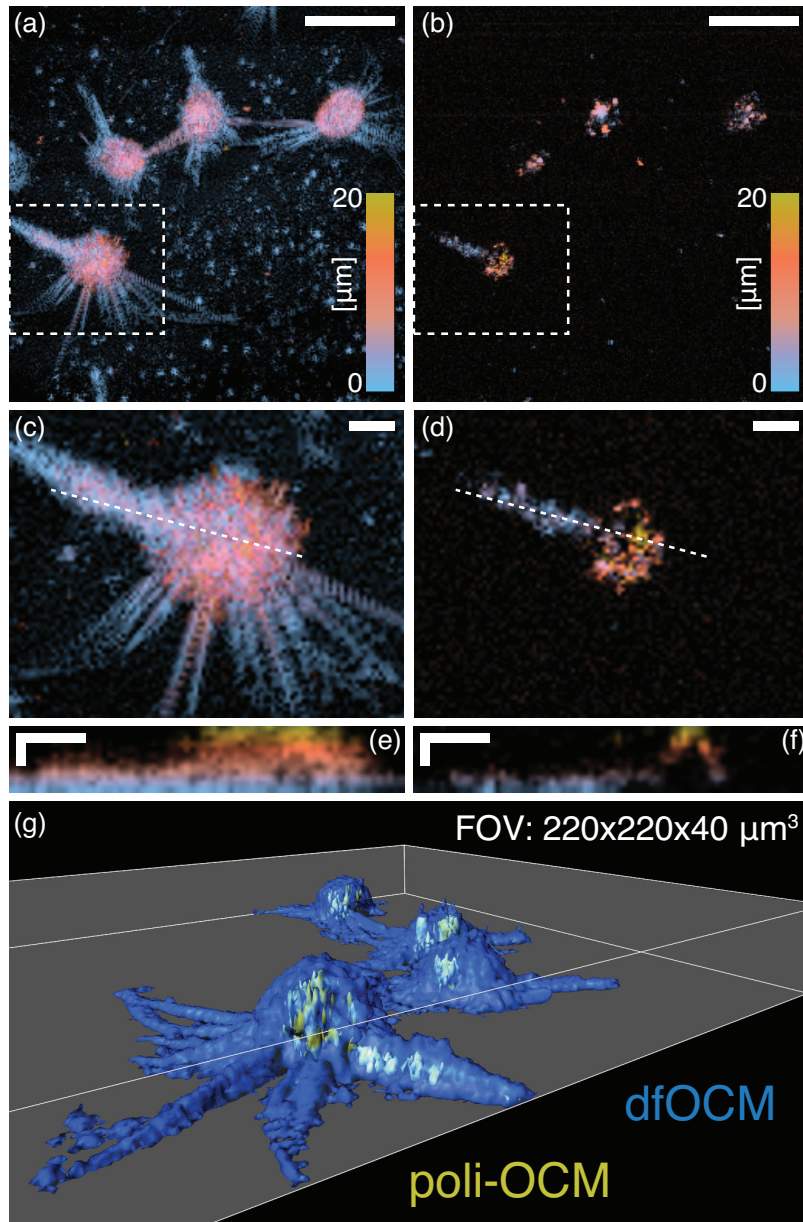


Fig. 6. Living HeLa cells loaded with 6 nm gold nanoparticles, en-face maximum projections of the depth color coded dfOCM (a) and poli-OCM (b) tomograms; (c, d) insets of (a) and (b); and cross-sections (e, f) along the lines depicted in (c) and (d); (g) 3D rendered superposition of dfOCM (in blue) and poli-OCM (yellow), see Media 1. $P_{\text{heat}}=12 \text{ mW}$, scale bars: $50 \mu\text{m}$ in (a, b) and $10 \mu\text{m}$ in (c, d, e, f).

used significantly lower intensities [20,21]. However, when considering the energy density, the current work features an advantage of at least one order of magnitude compared to previous OCT methods. For example, Skala et al. [20] applied 8 kW/cm² per A-scan with an integration time of 1 second, leading to 8 kJ/cm² for the detection of 60 nm particles in water. The limit of detection was located at 14 ppm, corresponding to 10 nanoparticles in the focal volume. Here, we employed 375 J/cm² for single 40 nm particles imaged with a SNR of 2500 (see Fig. 2).

Besides its ability to detect single particles, the main advantage of poli-OCM lies in its acquisition speed. In photothermal microscopy, as for any confocal microscope, the acquisition time for volumetric imaging increases dramatically as a scan in three dimensions is required. For example, a sampling of 200x200x30 points with a relatively short integration time of 250 μ s results in an acquisition time of 5 minutes, this extends to 20 minutes for a typical integration time of 1 ms. Obviously, such long integration times may not be suitable for functional imaging. In contrast, with an integration time of 250 μ s and a DOF of 50 μ m, poli-OCM records a tomogram of 200x200x30 voxels in 10 seconds. This is also significantly faster than any previous photothermal OCT setup where multiple acquisitions need to be performed at each sampling point, extending considerably the total acquisition time. Typical integration times are at least one order of magnitude slower than poli-OCM [20]. Moreover, none of these methods have shown single particle detection [19,21,22].

In the past, several labels and their dedicated detection schemes have been proposed for OCT [33]. Some labeling techniques not only provide a selective contrast but also information about the environment local to the probe, such as magnetomotive OCT [34], which is able to measure elastic properties of biological tissue [35]. In photothermal microscopy, the signal depends on the thermal characteristics of the medium and thus could provide some insight into the local properties of the sample. Another interesting option could be to make use of the spectral characteristics of specific compounds, e.g. hemoglobin, which offers the possibility of obtaining specific contrast without the addition of any contrast agent [10,11]. Thanks to this fast acquisition speed, the study of nanoparticles endocytosis could also be a well-suited application for combined dfOCM/poli-OCM imaging. The method's large DOF allows absorbing particles to be imaged over a range of several cell layers, and thus may also be applied for in-vivo biological studies.

Phototoxicity is a critical issue for any microscopy technique that requires significant light dose. This question was recently addressed by Wagner et al. [36] as they investigated the cell viability in function of the applied light dose during several cell growth cycles. At a wavelength of 514 nm, cells could experience a light dose of 100 J/cm² (cw) and still indicated natural cell viability. In the present work, an average light dose of 57.5 J/cm² at 532 nm was used in a sinusoidal regime, which remained well below the limit of 100 J/cm². Due to the weak near-infrared absorption of cells, we neglected the probe light phototoxicity.

6. Conclusion

In conclusion, we have introduced photothermal optical lock-in Optical Coherence Microscopy, a fast volumetric microscopy technique, able to image single gold nanoparticles in highly scattering medium with a 0.5 μ m lateral and 2 μ m axial resolution. Detection of single particles down to the size of 40 nm with a SNR of about 2500 was shown. Using a phantom sample prepared with gold colloids, a depth of field of 50 μ m was measured. In combination with dark-field OCM, the localization of 6 nm AuNPs inside cells in vitro was demonstrated. poli-OCM could become a versatile tool for functional cell 3D imaging.

Acknowledgments

This work was supported by the BetaImage Project (EU FP7-222980), funded by the European Commission within the 7th Framework Programme and by the Swiss National Science Foundation (grant 205321L-135353/1). We thank Prof. A. Grapin-Botton (Unité du Professeur Grapin-Botton, Ecole Polytechnique Fédérale de Lausanne, Lausanne, Switzerland) for kindly providing access to her cell culture facilities.